Molecular Therapy
Oncology
Original Article

The supramolecular processing of liposomal doxorubicin hinders its therapeutic efficacy in cells

Annalisa Carretta,[1] Aldo Moscardini,[1] Giovanni Signore,[2,3] Doriana Debellis,[4] Federico Catalano,[4] Roberto Marotta,[4] Valentina Palmieri,[5] Giulia Tedeschi,[6] Lorenzo Scipioni,[6] Daniela Pozzi,[7] Giulio Caracciolo,[7] Fabio Beltram,[1] and Francesco Cardarelli[1]

[1]Scuola Normale Superiore, Laboratorio NEST, Piazza San Silvestro 12, 56127 Pisa, Italy; [2]Biochemistry Unit, Department of Biology, University of Pisa, via San Zeno 51, 56123 Pisa, Italy; [3]Institute of Clinical Physiology, National Research Council, 56124 Pisa, Italy; [4]Electron Microscopy Facility, Istituto Italiano di Tecnologia (IIT), Via Morego 30, 16163 Genova, Italy; [5]Istituto dei Sistemi Complessi ISC CNR, Via dei Taurini 19, 00185 Rome, Italy; [6]Laboratory for Fluorescence Dynamics, Biomedical Engineering Department, University of California, Irvine, Irvine, CA, USA; [7]Department of Molecular Medicine, Sapienza University of Rome, Rome, Italy

The successful trajectory of liposome-encapsulated doxorubicin (e.g., Doxil, which has been approved by the U.S. Food and Drug Administration) as an anticancer nanodrug in clinical applications is contradicted by *in vitro* cell viability data that highlight its reduced efficacy in promoting cell death compared with non-encapsulated doxorubicin. No reports to date have provided a mechanistic explanation for this apparently discordant evidence. Taking advantage of doxorubicin intrinsic fluorescence and time-resolved optical microscopy, we analyze the uptake and intracellular processing of liposome-encapsulated doxorubicin (L-DOX) in several *in vitro* cellular models. Cell entry of L-DOX was found to lead to a rapid (seconds to minutes), energy- and temperature-independent release of crystallized doxorubicin nanorods into the cell cytoplasm, which then disassemble into a pool of fibril-shaped derivatives capable of crossing the cellular membrane while simultaneously releasing active drug monomers. Thus, a steady state is rapidly established in which the continuous supply of crystal nanorods from incoming liposomes is counteracted by a concentration-guided efflux in the extracellular medium of fibril-shaped derivatives and active drug monomers. These results demonstrate that liposome-mediated delivery is constitutively less efficient than isolated drug in establishing favorable conditions for drug retention in the cell. In addition to explaining previous contradictory evidence, present results impose careful rethinking of the synthetic identity of encapsulated anticancer drugs.

INTRODUCTION

The use of liposomes as delivery carriers for chemotherapeutic drugs offers a potential means to modulate drug distribution and final efficacy.[1] A paradigmatic case is the prototypical form of encapsulated doxorubicin, i.e., Doxil, the first nano-drug approved by the U.S. Food and Drug Administration (1995), currently used for the treatment of a number of pathologies, including AIDS-related Kaposi' sarcoma, recurrent ovarian cancer, metastatic breast cancer, and multiple myeloma (for a detailed review see Barenholz[2]). Doxil consists of 85-nm diameter liposomes with 2000-Da segments of poly-(ethylene glycol) (PEG) engrafted onto liposome surface and loaded with doxorubicin at a high concentration (i.e., approximately 2 mg/mL). As compared with non-encapsulated free doxorubicin (F-DOX), Doxil is endowed with at least two peculiar properties: (1) high stability in blood circulation, thanks to the protective lipid bilayer composed of high melting temperature phosphatidylcholine and cholesterol, and (2) preferential accumulation at the tumor site (approximately 10-fold higher as compared with normal tissue[3]) by exploitation of the so-called enhanced permeability and retention effect.[4] These properties, combined with the high drug-loading capacity inherent in liposomes, have significantly curtailed drug toxicity, particularly with regard to cardiac function.[5] Despite these undoubtedly positive characteristics, however, Doxil has not demonstrated unequivocal superiority over the non-encapsulated drug in terms of progression-free patient survival in phase 2/3 clinical trials[6–8]). *In vitro* tumor cell viability assays, in contrast, have indicated that a potential limitation to the efficacy of Doxil may reside at the cellular level,[9] specifically in its capability to release the active drug at the designated target site, the nucleus.[10,11] However, a comprehensive mechanistic understanding of the cellular and subcellular behavior associated with encapsulated doxorubicin remains conspicuously absent. To address this issue, here we exploit the intrinsic fluorescence properties of doxorubicin[12] and advanced microscopy techniques to monitor its uptake and intracellular fate, both encapsulated (in the form of Doxoves, a research-grade analog of Doxil,[13] hereafter referred to as liposome-encapsulated doxorubicin [L-DOX]) and non-encapsulated (F-DOX) in different *in vitro* cellular models. First, time-lapse confocal imaging

Received 4 April 2024; accepted 13 June 2024;
https://doi.org/10.1016/j.omton.2024.200836.

Correspondence: Francesco Cardarelli, Scuola Normale Superiore, Laboratorio NEST, Piazza San Silvestro 12, 56127 Pisa, Italy.
E-mail: francesco.cardarelli@sns.it

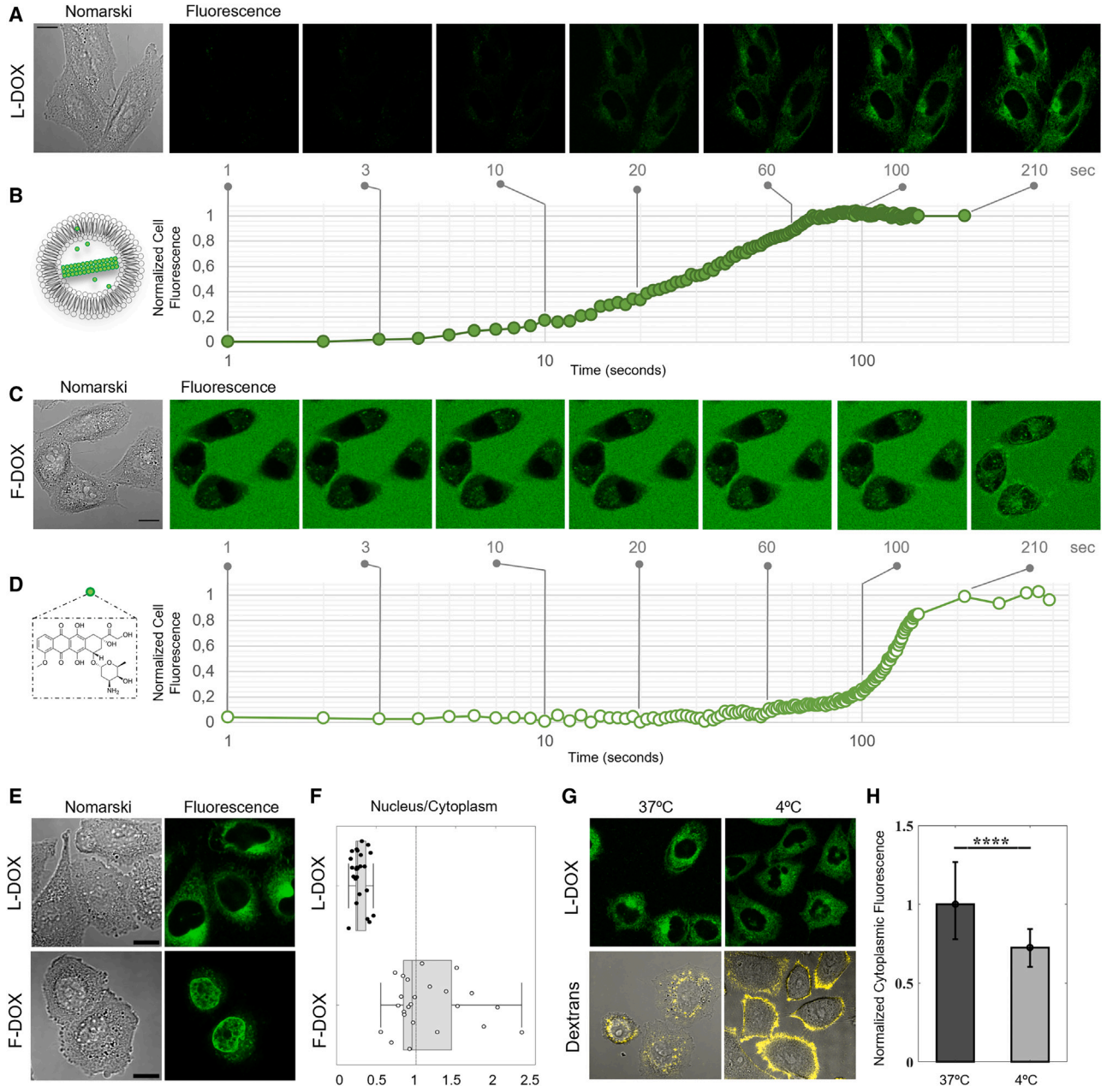

Figure 1. Cell entry kinetics and intracellular distribution of liposomal doxorubicin

(A) Exemplary micrographs were selected from a time-lapse confocal microscopy experiment conducted on CHO-K1 cells at a temporal resolution of 1 frame/s and under continuous exposure to the L-DOX. A diffuse fluorescence signal can be appreciated in the cell cytoplasm, rapidly increasing over time. Scale bar, 10 μm. (B) Plot of the intracellular fluorescence over time. Fluorescence is analyzed in the cell cytoplasm, then normalized by the total fluorescence for each frame (to correct for spurious intensity changes due, for instance, to changes of imaging focus, photo-bleaching, etc.) and, finally, normalized between 0 and 1 (see supplemental methods for more details). The plot shows that F-DOX entry into cells reaches a plateau after approximately 70 s from incubation. (C) Exemplary micrographs selected from a time-lapse confocal microscopy experiment conducted on CHO-K1 cells at a temporal resolution of 1 frame/s and under continuous exposure to F-DOX. F-DOX entry into cells, as compared with L-DOX, can be appreciated at later times (>100 s). Scale bar, 10 μm. (D) Plot of the intracellular fluorescence over time. Similarly to what was reported in (B), here fluorescence is analyzed in the cell, then normalized by the total fluorescence for each frame (to correct for spurious intensity changes due, for instance, to changes of imaging focus, photo-bleaching, etc.) and, finally, normalized between 0 and 1 (see supplemental methods for more details). The plot shows that F-DOX entry into cells reaches a plateau after approximately 200 s from incubation. (E) CHO-K1 cells incubated in the presence of either L-DOX (upper lane) or F-DOX (bottom lane) for 30 min, then rinsed and imaged by confocal microscopy. Scale bars, 10 μm. (F) Ratio of nuclear *vs*. cytoplasmic fluorescence intensity for each analyzed cell. Data were collected from $N = 3$ independent experiments and are presented as box plots with whiskers corresponding to the 'min' and 'max' values found, the central line corresponding to the median value of the

(legend continued on next page)

of cells exposed to L-DOX in different conditions reveals that its uptake is fast (seconds), and temperature and energy independent. Contrary to F-DOX, however, L-DOX's fast and passive uptake does not result in effective nuclear accumulation of the drug, which instead remains mostly localized within the cytoplasm. To understand this result, fluorescence lifetime imaging microscopy (FLIM) was used as a tool with exquisite sensitivity to the supramolecular organization of the emitter, i.e., the drug itself.[14] The characteristic FLIM signature of the cytoplasm of cells exposed to L-DOX is compatible, at early times, with the presence of a dominant species made of drug nanorod crystals. Such signature then evolves over time (i.e., minutes to hours) as the cytoplasmic reservoir of nanorods of crystallized doxorubicin progressively disassembles into a pool of fibril-shaped derivatives capable of crossing and interacting with the cellular membrane, while concomitantly releasing active drug monomers. Therefore, a steady state is rapidly established, in which the continuous supply of crystal nanorods from incoming liposomes is counterbalanced by the concentration-guided efflux toward the extracellular medium of all drug species, including active drug monomers. These results clearly underscore how liposome-mediated cellular delivery of doxorubicin, although fast and temperature independent, does not establish the conditions for extensive accumulation of the active drug in the desired target compartment, the cell nucleus.

RESULTS

Cell entry kinetics and intracellular distribution of liposomal doxorubicin

Here we use liposomal doxorubicin in the form of Doxoves (L-DOX) as compared with F-DOX. Based on the manufacturer's indications, L-DOX comes with most of the drug molecules (>98%) encapsulated within the aqueous liposome lumen in the form of a nanorod-shaped crystal (confirmed by cryo-electron microscopy [EM] analysis) (Figure S1); in addition, as demonstrated by some of us using label-free optical microscopy,[14] the remaining fraction of the drug (<2%) comprises free-in-solution doxorubicin molecules (either encapsulated or non-encapsulated) and doxorubicin molecules associated with both leaflets of the liposomal membrane. In spite of this in-depth knowledge of L-DOX supramolecular organization *in cuvette* (or synthetic identity), an accurate understanding of its intracellular processing and fate (or biological identity) has remained elusive thus far and is elucidated in this work. To commence, by exploiting the well-known intrinsic fluorescence of doxorubicin,[12] we perform time-lapse confocal microscopy of drug uptake in cells exposed to L-DOX as compared with control ones exposed to F-DOX (Figure 1). In the experiment reported in Figure 1A, L-DOX is administered to living CHO-K1 cells at approximately 10 μg/mL drug concentration and confocal snapshots are taken at a temporal resolution of approximately 1 image per second, under continuous exposure to the drug (no rinsing). Inspection of confocal images shows that the intracellular accumulation of L-DOX affects the cell cytoplasm with no detectable involvement of the nuclear compartment (complete time-lapse is included as Video S1). In terms of kinetics, cytoplasmic fluorescence increases rapidly over seconds and reaches a plateau level just over 60 s after administration of the drug. The plateau level is then maintained across minutes (in this example approximately 5 min) (full green dots in Figure 1B). If the drug is administered to cells in non-encapsulated form, it is still capable of entering cells (Figure 1C and Video S2), as fully expected based on previous reports,[15] but with significantly slower characteristic kinetics (empty green dots in Figure 1D); indeed, F-DOX intracellular levels reach a plateau only approximately 200 s after administration. Of particular note, the two drug formulations show clear differences also in terms of final localization within cells: while L-DOX remains exclusively localized within the cytoplasm, F-DOX effectively reaches the nucleus, its intended target. This can be better appreciated by removing excess drug from the medium and reiterating imaging of cells, as reported in Figure 1E alongside statistics of the nucleus/cytoplasm fluorescence ratio from multiple cells (Figure 1F). Similar results are reproduced in two additional cell lines, MDA-MB-231 and MCF10A (Figure S2). To understand whether the intracellular plateau levels reached by L-DOX effectively correspond with a steady state between drug entering and exiting the cell, we performed a control experiment in which L-DOX is removed from the cell medium by rinsing after the plateau is reached and cells are followed in time: under these conditions, as reported in Figure S3, the intracellular drug content exits into the extracellular medium in minutes (mirroring its entry), demonstrating its membrane-crossing capabilities. The observed marked difference in uptake is expected as L-DOX and F-DOX are exploiting different mechanisms of cell entry. In fact, it is well known that F-DOX enters cells by concentration-guided passive diffusion across the cell membrane, a route not available for large PEGylated liposomes, which instead are known to enter cells by either energy-dependent endocytosis or energy-independent direct fusion of the liposome with the cell plasma membrane.[16] The control experiments reported in Figures 1G and 1H show that L-DOX entry is mostly energy independent, as it occurs also at 4°C or in the absence of ATP (Figure S4). In keeping with these observations, a combination of transmission EM (TEM) analysis (Figure S5) and fluorescence-based co-localization assays (Figure S6) highlights a minor contribution of the endocytic pathway and involvement of lysosomes as a final sub-cellular target for this route.

Phasor-FLIM signature of intracellular L-DOX: From synthetic to biological identity

Based on the results so far and on the available literature,[16] it can be reasonably hypothesized that L-DOX entry into cells is dominated by direct fusion of the liposome with the plasma membrane and

distribution, and the limits of the box to the 25th and 75th percentiles. (G) The uptake of L-DOX (top lane) and FITC-labelled 70-kDa dextrans (bottom lane) was monitored in CHO-K1 cells at 37°C (left column) and 4°C (right column). Scale bars, 10 μm. (H) Normalized cytoplasmic fluorescence from cells exposed to L-DOX at 37°C or 4°C. Data at the two temperatures were acquired in two consecutive experiments to maintain all the acquisition parameters constant, and are presented as Mean ± SD. Data were compared using Welch's t test ('****' corresponds to p value < 0.0001).

subsequent release of liposomal content into the cytoplasm. The peculiar increase in fluorescence brightness of L-DOX upon cell entry as compared with F-DOX (see images in Figures 1A and 1C) further supports this hypothesis, as it entails a swift reorganization of the synthetic identity of the drug, from the highly fluorescence-quenched form in the extracellular medium (i.e., nanorod crystals trapped within intact liposomes) to the form released, and eventually processed, within the intracellular environment (i.e., nanorod crystals within the cell cytoplasm). To get an experimental demonstration of this hypothesis, we exploit the high sensitivity of fluorescence lifetime to the supramolecular organization of the emitter, i.e., the drug itself, and its potential to discriminate multiple species co-occurring in the sample (and even in the same pixel), as recently demonstrated.[14,17–19] Phasor plot-based representation of lifetime data is used as fit-free graphical tool for data visualization and analysis (see materials and methods for further details). First, due to their structural differences, we expect nanorod crystals released into the cell cytoplasm to have a lifetime signature different from both that of intact L-DOX and that of F- DOX. As reported in Figure 2A and in Tentori et al.,[14] three distinct species, corresponding with free, liposome-interacting, and crystal-form doxorubicin (DOX_f, DOX_b, and DOX_c) contribute to generate the lifetime signature of L-DOX. In contrast, under the imaging conditions used, cells possess their own autofluorescence with respective lifetimes, as reported in Figure S7. If we assume that L-DOX enters the cell without changing its synthetic identity, then its phasor FLIM signature would be expected to appear on the segment connecting the lifetime signatures of intact L-DOX (full gray dot in Figure 2B) and of cell autofluorescence (full white dot in Figure 2B). Instead, consistent with our hypothesis that L-DOX does not maintain its synthetic identity upon entry into the cell cytoplasm (Figure 2C), the experimentally measured phasor FLIM signature of L-DOX in the cell cytoplasm after 30 min of exposure is markedly modified. Careful inspection of the L-DOX phasor-cluster position and shape suggest the existence of differential interactions of the drug released into the cytoplasm with the heterogeneous landscape of intracellular membranes, in turn probably responsible for the corresponding lifetimes coming out of the reference triangle in the phasor plot (see further cluster analysis in Figure S8). Please note that L-DOX phasor signature is highly reproducible among different cells in the same experiment (see cluster analysis in Figure S9). At the same time, the L-DOX intracellular phasor signature excludes the possibility that the monomeric drug (F-DOX) is being released from internalized liposomes at this early time. Indeed the synthetic identity of F-DOX (mono-exponential on the universal semi-circle, Figure 2D) combines as expected with cell auto-fluorescence lifetime, producing a cluster that is also further modified by the well-characterized interaction of F-DOX with intracellular players, mainly membranes in the cytoplasm and DNA in the nucleus[20,21] (Figure 2F; see Figure S10 for further analytical considerations on F-DOX intracellular lifetime distribution). Please note that analogous results are obtained in MDA-MB-231 and MCF10A cells (Figure S11). To sum up: the phasor FLIM signature of L-DOX in cells is modified with respect to the pristine drug, but not toward the release of monomeric doxorubicin. At this point, it remains to be demonstrated whether the intracellular phasor FLIM signature of L-DOX may be compatible with that of nanorod crystals poured into the cytoplasm upon liposome fusion with the cell membrane. To this end, we disrupted the integrity of the membrane of L-DOX liposomes by sonication (Figure 2G), thus mimicking *in cuvette* what happens to the crystal nanorod upon L-DOX fusion with the cell membrane and crystal nanorod release into the cytoplasmic aqueous solution.[22] Of note, upon administration to cells, the products of L-DOX sonication rapidly enter the cell, in keeping with the membrane-crossing capabilities already characterized for the material poured by L-DOX into cells (Figure S3) and exclusively localize within the cytoplasm (Figure 2H). Finally, their phasor-FLIM signature in cells resembles what was observed in L-DOX-treated cells at early times (Figure 2I; for *in cuvette* characterization refer to Figure S12).

Time evolution of L-DOX biological identity: The role of fibrillary aggregates and the path of the monomeric drug to the nucleus

The phasor FLIM signature of L-DOX in the cell cytoplasm at early times complies well with the hypothesis of liposome fusion with the plasma membrane and release of its content into the cell. At this point, it remains to be demonstrated whether the released material (i.e., nanorod crystals) eventually evolves over time into some other drug form. In this regard, we recently demonstrated that L-DOX synthetic identity evolves spontaneously *in cuvette* at 37°C[23] (top-down approach, schematics in Figure 3A) generating drug products with an FLIM signature *in cuvette* (Figure S13) compatible with that measured after sonication (Figure S12). Upon administration to cells, the products of L-DOX spontaneous evolution, similar to those obtained by sonication, show the ability to cross the cell membrane and localize exclusively in the cytoplasm (see an exemplary image in Figure 3B) with a phasor FLIM signature coincident to that of L-DOX in cells at early times (Figure 3C). To get direct imaging of the drug species endowed with these properties, negative staining EM on the spontaneously evolved L-DOX is performed. This analysis shows that fibrillary-shaped structures are present massively in the sample at the end of the evolution process both inside and outside liposomes (Figure 3D). These fibrillary structures present a characteristic thickness approximately 10-fold smaller than the intact nanorod (Figure 3E; 2.9 ± 1.0 nm, blue trace, as compared with 22.5 ± 5.1 nm, black trace; refer to Figure S14 for negative-staining EM performed on intact L-DOX at 4°C). This result is not entirely surprising, as it was already demonstrated by cryo-TEM that the liposome-carried crystal is composed of fibrous crystals with a diameter of approximately 2.4 nm associated together to form the nanorod.[24] To unambiguously attribute the observed properties to such fibrillary structures, we produced them *in cuvette* in a controlled manner, by means of a well-established bottom-up protocol[25] (schematics in Figure 3F and *in cuvette* FLIM analysis in Figure S15). As reported in Figure 3G, negative-staining EM confirms that fibrils are formed by this procedure and have the expected thickness (2.9 ± 0.8 nm, red trace in Figure 3H) with respect to the intact nanorod (22.5 ± 5.1 nm, black trace as before). Once administered to cells, these fibrils enter cells and accumulate in the cell cytoplasm (with no nuclear signal)

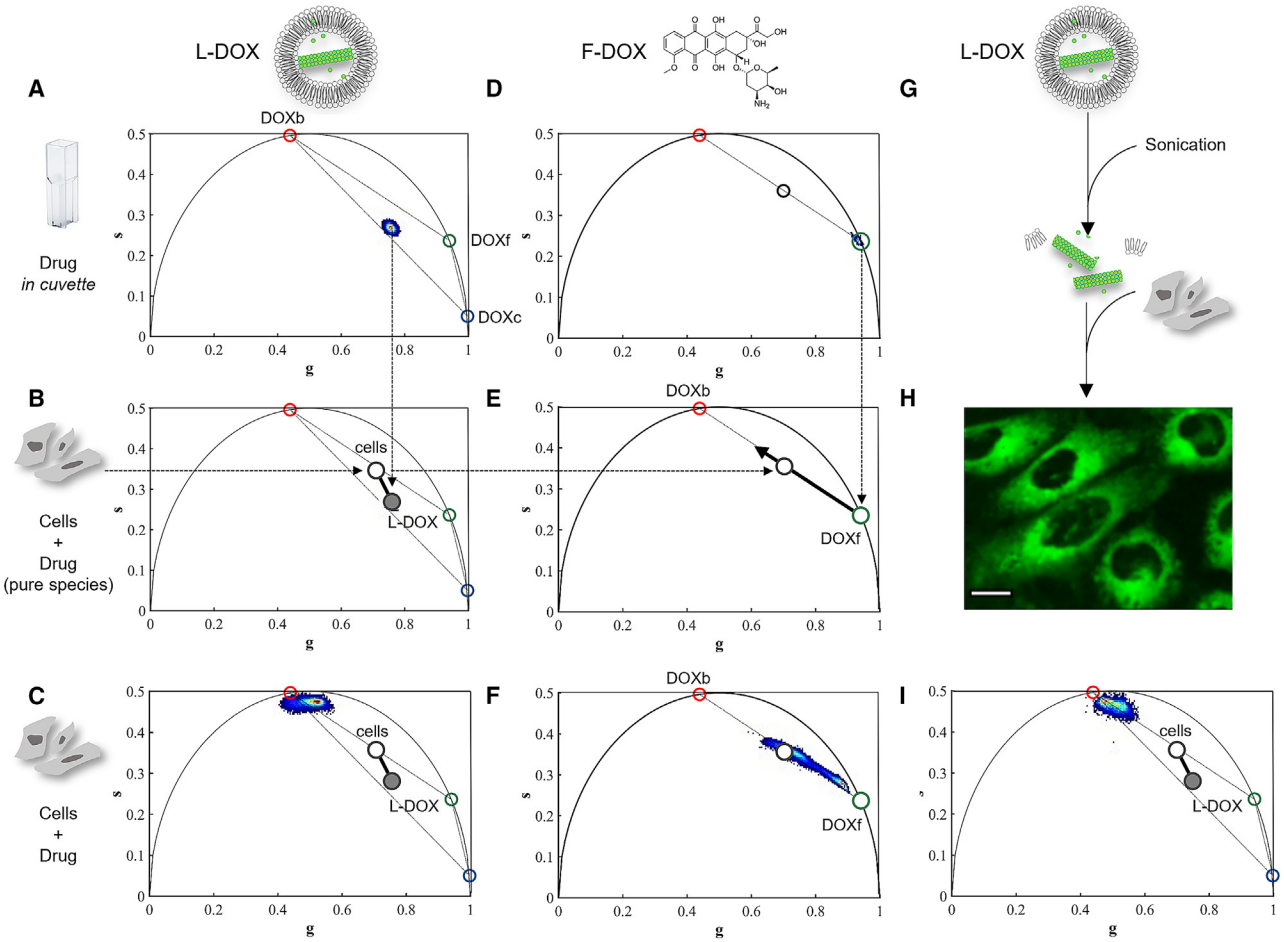

Figure 2. Phasor FLIM analysis of intracellular L-DOX

(A) Exemplary phasor FLIM analysis of intact L-DOX in aqueous solution: the characteristic lifetime is multi-exponential, as it is the result of the fractional contribution of three constituent species, i.e., crystallized DOX (DOX_c), free-in-solution DOX (DOX_f), and DOX interacting with the liposome membrane (DOX_b). (B) Upon administration to cells, the characteristic phasor-FLIM signature of L-DOX in aqueous solution reported in (A) (gray full dot) is expected to combine with the intrinsic cell autofluorescence lifetime (characterized in Figure S7 and reported here as a white dot), thus appearing on the segment (in black) between the two pure species. (C) By contrast, the obtained phasor FLIM signature of L-DOX in the cytoplasm (at 30 min of incubation) is not localized on the expected segment but close to the characteristic FLIM signature of DOX interacting with membranes ('DOX_b', red empty dot). The cluster seems t be elongated, suggesting the differential contribution of multiple species within the cell cytoplasm (refer to the main text and Figure S8 for further cluster interpretation and analysis). (D) Exemplary phasor FLIM analysis of F-DOX in aqueous solution: the characteristic lifetime is mono-exponential, at approximately 1.0 ns on the universal semi-circle. (E) Upon administration to cells, the characteristic phasor-FLIM signature of F-DOX in aqueous solution reported in (D) (green empty dot) is expected to combine with the intrinsic cell autofluorescence lifetime (characterized in Figure S7 and reported as a white dot), and, eventually, with the lifetime of DOX interacting with membrane lipids (DOX_b, red empty dot), i.e., lying on the segment encompassing F-DOX, cell, and DOX_b characteristic lifetimes, in a position that depends on the fractional contribution of each species. (F) In keeping with the expectations described in (E), the F-DOX phasor FLIM signature in cells is elongated along the segment encompassing the three putatively contributing species (refer to Figure S10 for further cluster analysis). (G) Schematics of L-DOX dissolution by sonication. (H) Exemplary FLIM image of cells exposed to the products of L-DOX sonication for 30 min. Scale bar, 10 μm. (I) The products of L-DOX sonication are characterized by a phasor FLIM signature in cells that closely resembles that of L-DOX (compare with C) and is markedly different from either L-DOX remaining intact (B) and F-DOX in cells (F).

(Figure 3I) while showing a cytoplasmic phasor FLIM signature close to that observed in L-DOX-treated cells at early times (Figure 3L). Taken together, these control experiments suggest that doxorubicin fibrillary aggregates may represent a reasonable intermediate during the intracellular processing of the L-DOX-carried crystal nanorod. The intracellular properties of the fibrillary aggregates observed here well comply with previous reports in which fibrillary doxorubicin aggregates of various linear sizes (even as small as dimers) were able to enter cells but not able to accumulate in the nucleus, thus resulting in reduced cytotoxic effects if compared with monomeric doxorubicin.[25,26] It is interesting to note that fibrils probed as pure species (bottom-up experiment) have a characteristic *in cuvette* lifetime close to that of monomeric F-DOX (i.e., almost mono-exponential at approximately 1.0 ns); this in turn demonstrates that only

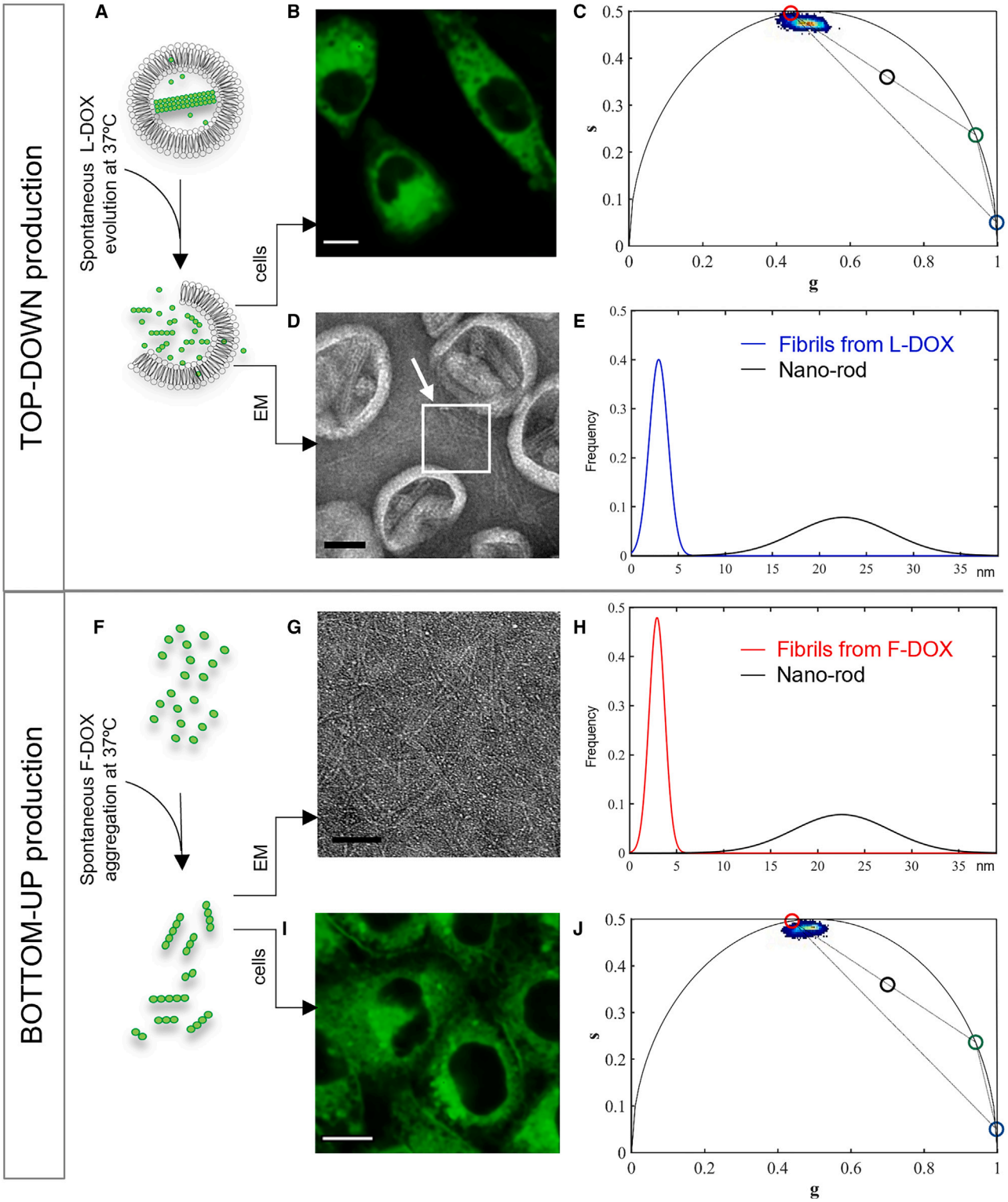

Figure 3. The role of fibrillary DOX aggregates

(A) Schematic representation of L-DOX undergoing spontaneous evolution upon incubation at 37°C. (B) Upon administration to cells and 30-min incubation, the products of spontaneous L-DOX evolution yield the same characteristic intracellular localization reported for L-DOX at early times (as for L-DOX sonication products), i.e., accumulation in

(legend continued on next page)

the juxtaposition of multiple fibrils to form a rod, as in the intact drug, generates fluorescence quenching and therefore a reduced lifetime. At this point, to clarify whether monomeric doxorubicin may be released from intracellular fibrils at later times, we performed an FLIM experiment at different time points, in a time window of 24 h and under continuous exposure of cells to L-DOX. Exemplary FLIM images collected at different time points (i.e., 1, 6, and 18 h of continuous exposure) are reported in Figure 4A. It is worth noting that the phasor FLIM signature of the drug does evolve significantly over time (see the phasor cluster position and shape in Figure 4B). In more detail, the phasor cluster (left) elongates toward shorter lifetimes progressively over time; of particular note, after 18 h of continuous exposure, the cell nucleus shows the characteristic phasor signature of the monomeric drug intercalated into chromatin (Figures 4B–4D, bottom panel to compare with Figure S10), which is slightly tilted with respect to the expected reference segment, in keeping with previous observations on the lifetime of chromatin-intercalated doxorubicin.[20,21] In keeping with lifetime-based observations, a detectable amount of fluorescence is observed in the cell nucleus after 18 h of continuous exposure (see Figure 4A, bottom).

DISCUSSION

Our results demonstrate that monomeric DOX is gradually released from the nanorod crystals and is able to reach the nucleus, albeit on a timescale markedly slower compared with that of the non-encapsulated drug. This result complies well with the known reduced cytotoxic effects of L-DOX, with respect to F-DOX, in cultured cells under a typical 24-h incubation assay, as also confirmed here for all the cell lines tested (see viability tests in Figure S16). Overall, data support the model schematically represented in Figure 5. F-DOX, on one hand, enters cells *via* passive membrane permeation,[27] exploiting the favorable concentration gradient (Figure 5i, unidirectional arrows at early times), rapidly reaches the nucleus and intercalates into DNA. It is known that F-DOX reaches a DNA-binding saturation level equivalent to approximately one molecule every five base pairs on the DNA strand[28]; the main pharmaceutical activity is then exerted by inhibition of topoisomerase II and stabilization of the ternary drug-topoisomerase II-DNA complex, which leads to DNA damage and the induction of apoptosis.[29] F-DOX molecules not involved in DNA binding spread across the cytoplasm and other organelles, contributing to cell death by a number of different mechanisms, which include membrane potential impairment, potentiation of free radical formation, and oxidative damage.[30] An overall stationary state of F-DOX intracellular distribution is eventually reached when passive entry is counterbalanced by exit, either passive or by active-pumps-mediated transport[31] (Figure 5ii, bidirectional arrows at later times). In contrast with F-DOX, L-DOX accumulates in the cell cytoplasm with no detectable signal in the nucleus at early times (i.e., seconds to minutes) (Figure 5, bottom). As measured by timelapse confocal imaging, the cell uptake of L-DOX is dominated by a fast and passive route of entry, presumably mediated by the direct fusion of the liposome with the plasma membrane and release of the crystallized drug into the cytoplasm (Figure 5iii). By a combination of top-down and bottom-up strategies to mimic what may happen to the crystal nanorod upon release into the cytoplasm, we support the hypothesis that the intracellularly released crystal progressively disassembles into fibrillary-shaped derivatives, a supramolecular conformation of doxorubicin already observed by others[26] and endowed with peculiar intracellular distribution/transport properties, including the ability to interact with membranes, but not to intercalate into DNA[25] (Figure 5iv). In addition, as measured by a combination of TEM and fluorescence-based co-localization experiments, a fraction of drug-loaded liposomes may enter by endocytosis and proceed toward trapping/degradation within lysosomes (Figure 5v, violet arrows). While TEM does not permit the exact identification of the specific endocytic route under examination, the distinctive size distribution of the vesicles (ranging from 300 to 600 nm, exhibiting high variability) and their ultrastructural attributes are consistent with those of vesicles from macropinocytosis,[32] a route deputed for the delivery of material to the lysosome. In this regard, Seynhaeve and co-authors[10] already observed the localization of both doxorubicin and its liposomal carrier in the lysosomal compartment, while Yang and co-authors[33] proposed an additional contribution from energy-dependent clathrin-mediated endocytosis, a mechanism that does not exclude final entrapment within lysosomes. It is worth noting that neither of these reports highlighted the role of liposome fusion with the cell membrane in L-DOX entry. A reasonable explanation may be linked to the use of extensive cell washing before imaging, which may have favored drug redistribution outside the cell (as demonstrated here). In general, the marked cytoplasmic retention of the liposome-carried drug observed here, besides being in keeping with the reduced cytotoxicity in cultured cells, contributes to explaining the recent observation that liposomal DOX triggers cell death via effectors located in the cytoplasm (e.g., apoptosis via caspase 3 activation), in addition to those located in the nucleus (e.g., necrosis via caspases-independent mechanisms[11]). Also, it complies well with recent

the cell cytoplasm with no detectable signal from the nucleus (exemplary FLIM image; scale bar, 10 μm). (C) Phasor-based analysis of the FLIM acquisition in (B) yields a lifetime distribution in the phasor plot that closely resembles the one reported for L-DOX at early times (as for L-DOX sonication products). (D) Negative-staining EM micrograph of L-DOX after spontaneous evolution at 37°C shows the appearance of fibril-shaped structures both inside and outside liposomes. Scale bar, 50 nm. (E) Thickness comparison between the fibrils obtained by spontaneous evolution of L-DOX and the intact nanorod, as measured on L-DOX maintained at 4°C. (F) Schematic representation of the bottom-up process by which fibrils are obtained upon incubation of F-DOX at 37°C. (G) Negative-staining EM micrograph of doxorubicin fibrillary aggregates obtained bottom-up starting from F-DOX. Scale bar, 50 nm. (H) Thickness comparison between the fibrils obtained bottom-up from F-DOX and the intact nanorod, as measured on L-DOX maintained at 4°C. (I) Upon administration to cells and 30-min incubation, the fibrils obtained bottom-up from F-DOX yield the same characteristic intracellular localization reported for L-DOX at early times (as for L-DOX sonication products and for products of L-DOX spontaneous evolution), i.e., accumulation in the cell cytoplasm with no detectable signal from the nucleus (exemplary FLIM image; scale bar, 10 μm). (J) Phasor-based analysis of the FLIM acquisition in (I) yields a lifetime distribution in the phasor plot that closely resembles the one reported for L-DOX at early times (as for L-DOX sonication products and for products of L-DOX spontaneous evolution).

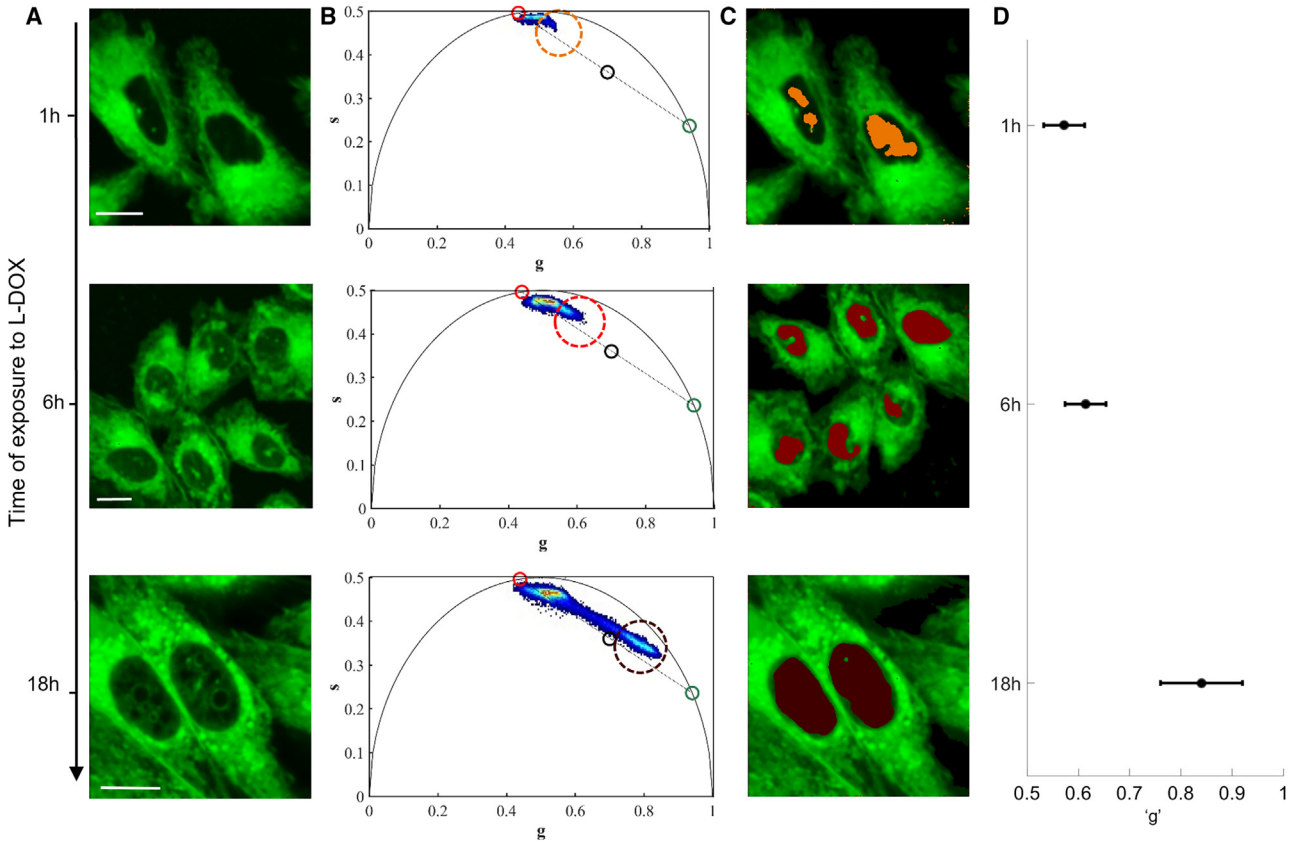

Figure 4. Time evolution of the phasor-FLIM signature of L-DOX

(A) Exemplary FLIM images obtained upon continuous exposure of cells to L-DOX for 1 h (top), 6 h (middle), and 18 h (bottom). Scale bars, 10 μm. (B) Phasor-based analysis of the measured lifetimes: the cluster corresponding to intracellular pixels progressively elongates toward shorter lifetimes with increasing incubation times, in particular toward the characteristic position of the nucleus already observed in F-DOX-treated cells. (C) The cursors applied in (B) to the phasor plot highlight pixels corresponding to the nuclear compartments, which are here color-coded accordingly. The characteristic lifetime of the nuclear compartment evolves, being always the combination of the lifetime of DOX molecules (which are eventually present in the nucleus and intercalated into DNA) and the lifetime of cytoplasmic DOX from out-of-focus planes. (D) Temporal evolution of the characteristic '*g*' coordinate of the barycenter of the phasor cluster corresponding to the nuclear compartment. Data are presented as Mean ± SD values.

findings by some of us on a liposomal formulation analogous to Doxil, but containing the anticancer drug Irinotecan.[34] FLIM investigations extended on a larger time window, i.e., from minutes to hours, reveal here that monomeric active doxorubicin is effectively released from the fibrillary derivatives and is able to reach the nucleus and intercalate into DNA (Figure 5-*vi*). Yet, the efficiency of this process cannot be higher than that observed in cells exposed to the same amount of non-encapsulated drug (F-DOX); in fact, while the cytoplasm of cells exposed to L-DOX is constantly filled with crystal derivatives by incoming liposomes, it equally constantly loses material (both fibrillary and monomeric) that exits the cell owing to its intrinsic membrane-crossing capabilities and to a favorable concentration gradient (i.e., please note that the extracellular medium does not contain crystal derivatives but only intact liposomes) (Figure 5vii). The final picture is that liposome-mediated cellular delivery of doxorubicin, although fast and temperature independent, is constitutively unable to establish the conditions for extensive accumulation of the active drug in the nucleus.

We are tempted to speculate that similar conditions might also affect drug effectiveness at the tumor site during systemic *in vivo* applications, negatively impacting the amount of drug that can reach the nucleus of tumor cells. This overlooked factor, in fact, may exacerbate the adverse impact of the protein corona on liposome stability *in vivo*,[35] it may potentially add to the leakage of the drug from liposomes already postulated *in silico*[36] and characterized by *in vitro* experiments under tumor interstitial fluid-mimicking conditions[37] and, more in general, it may well comply with the rapidly changing paradigm of nanoparticle retention at the tumor site.[38] It is undoubted that future investigations should contemplate optimizing the synthetic identity of the drug to obtain effective retention at the tumor site but, as emerging here, also at the cellular level.

MATERIALS AND METHODS

Materials

Doxoves (F30204B-D2) was purchased from FormuMax Scientific and stored at 4°C. It consists of HSPC/CHOL/mPEG2000-DSPE

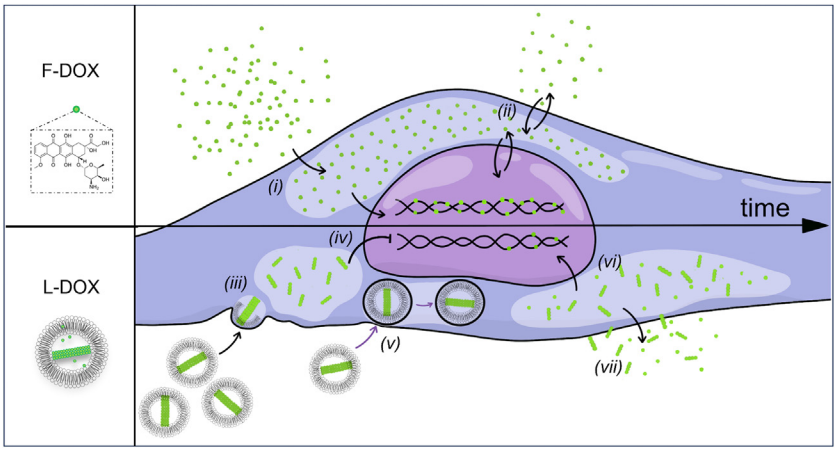

Figure 5. Schematic model of L-DOX cell entry and processing as compared with F-DOX

In the top, a cell interacts with F-DOX: at early times (i) F-DOX enters by passive diffusion up to the nucleus, while at later times (ii) a dynamic equilibrium is established. In the bottom, a cell interacting with L-DOX: materials just released upon the direct fusion of the liposome with the plasma membrane (iii) are not able to enter the nucleus (iv). L-DOX can also enter by endocytosis (v). At later times, fibrillary derivatives release monomeric active doxorubicin capable of reaching the nucleus (vi); both exit the cell due to a concentration gradient (vii).

liposomes, loaded with 2 mg/mL doxorubicin and dissolved in the manufacturer's buffer containing 10 mM histidine and 10% sucrose at a pH of 6.5. Doxorubicin hydrochloride was purchased from Sigma Aldrich as powder, then dissolved in water at a concentration of 2 mg/mL and stored at −20°C. Doxorubicin hydrochloride for crystal production was purchased from Thermo Fisher Scientific, dissolved in water at a concentration of 10 mg/mL, and stored at −20°C.

Cell culture and treatments

CHO-K1 cells (CCL-61 ATCC) were cultured in DMEM/Nutrient Mixture F-12 without phenol red (DMEM/F-12, Gibco), supplemented with 10% fetal bovine serum (FBS) (Gibco), 4 mM L-glutamine, 100 U/mL penicillin, and 100 μg/mL streptomycin (Invitrogen). Cells were seeded on 22-mm glass bottom dishes (WillCo Wells) and allowed to adhere overnight, maintained in a humidified incubator at 37°C and 5% CO_2 atmosphere. Cells were cultured until 70%–80% confluence and then treated with F-DOX/L-DOX or fluorophores for imaging. Human mammary epithelial cells MCF10A were grown in DMEM (Merck KGaA)/Ham's F12K (Thermo Fisher Scientific) medium (1:1) containing 5% horse serum, 1% penicillin/streptomycin, 2 mM L-glutamine, 10 μg/mL insulin, 0.5 μg/mL hydrocortisone, 50 ng/mL cholera toxin (all from Merck KGaA), and 20 ng/mL epidermal growth factor (PeproTech). MDA-MB231 cells were cultured in DMEM medium (DMEM, high glucose, with l-glutamine, GenClone), supplemented with 10% v/v FBS (heat-inactivated FBS, GenClone) and 1% v/v penicillin/streptomycin solution 100× (1,0000 U penicillin and 10 mg/mL streptomycin in 0.85% saline solution, GenClone), in a 37°C and 5% CO_2 incubator.

Cell viability tests

MTT assay (Biotium) was performed according to the manufacturer's specifications. Briefly, cells were seeded at 10,000 cells per well in 96-well plates and left overnight to attach. The following day, the culturing medium was replaced with a culturing medium containing doxorubicin or Doxoves in various concentrations. We added 10 μL MTT solution 24 h later to each well for 3 h, after which 200 μL of DMSO was added to each well. Absorbance was measured with a plate reader at 570 nm and 630 nm. As doxorubicin and Doxoves have non-negligible absorbance at high concentrations, we prepared a further 96-well plate with only culturing medium in the same conditions, without adding MTT, that was measured with the same parameters. Data were analyzed as follows. (1) Absorbance at 630 nm was subtracted from the absorbance at 570 as suggested by the manufacturer for MTT background correction (background-corrected absorbance). (2) The average background-corrected absorbance from the well containing only media and drugs was subtracted from the samples with cells (corrected absorbance). (3) Viability was expressed as a percentage of the average corrected absorbance of the controls (no drugs added).

Live cell imaging

Confocal fluorescence imaging on CHO-K1 cells was performed on a Zeiss Axio Observer 7 confocal microscope with a 40×, 1.3-NA oil immersion objective. All experiments (except those at low temperatures) were carried out at 37°C using an incubation chamber with a controlled CO_2 supply. In the absence of additional fluorophores, doxorubicin fluorescence was elicited by exciting at 488 nm (Argon laser) and collected in the 500- to 700-nm optical window. Sequential images for live monitoring of L-DOX were taken for approximately 3–4 min focusing on the same area at a temporal resolution of one image per second. Sequential imaging started with a lag time of approximately 10 s from drug administration (performed directly under the microscope), which served to adjust the imaging focus on the selected cell. Image analysis was performed using ImageJ. For intensity calculation, the transmitted light image was used to draw the region of interest (i.e., nucleus or cytoplasm or entire cell). To analyze the kinetics of cell uptake of L-DOX and F-DOX, the cytoplasmic fluorescence (entire cell in the case of F-DOX) was normalized by means of the total fluorescence measured in the image to correct first for spurious changes of fluorescence intensity due, for instance, to changes of the imaging focus, phot-bleaching, etc. Then, fluorescence was normalized between 0 and 1, first by subtracting the initial fluorescence value and then dividing by the final plateau intensity value (estimated by averaging the last points). For co-localization experiments, Lysotracker DeepRed (Invitrogen) stock solution was diluted to 70 nM final concentration in the growth medium. To highlight doxorubicin presence in lysosomes, cells were previously incubated for 2 h with

F-DOX or L-DOX. After rinsing, their medium was replaced with the lysotracker-containing medium. The observation started after 20 min at a Zeiss Axio Observer 7 confocal microscope equipped with a 40×, 1.3-NA oil immersion objective. Lysotracker-DeepRed fluorescence was excited at 640 nm and collected above 645 nm, while doxorubicin was excited as described above. For image analysis, the Jacop plugin of ImageJ was used. Confocal imaging on MCF10A and MDA-MB-231 cells was performed by using an Olympus FluoView FV1000 system with IX81 microscope body and two-photon excitation using a Spectra-Physics MaiTai HP laser and Fast-FILM-box (ISS, Inc). The samples were observed by a pulsed diode laser operating at 80 MHz with an excitation wavelength of 760 nm. The emission was collected in the 470- to 720-nm range by a filter block composed of a dichroic mirror 470 nm long-pass filter and a 720 short-pass filter.

Energy depletion experiments

The role of endocytosis in L-DOX entry was first studied by incubating CHO-K1 cells (already stored in ice for 1 h) at 4°C for 30 min with 12 μg/mL liposomal doxorubicin. To confirm the inhibition of endocytosis at low temperatures, fluorescein isothiocyanate-dextran 70 kDa (Invitrogen) was used to label macropinosomes. CHO-K1 cells were incubated at the desired temperature (4°C or 37°C) for 30 min in a medium containing 1 mg/mL fluorescein-labelled dextran and then washed with DPBS. Confocal fluorescence images were acquired with a Zeiss Axio Observer 7 confocal microscope equipped with a 40×, 1.3-NA oil immersion objective. Dextran's fluorescence was excited at 488-nm (Argon laser) and collected in the 450- to 520-nm range. Data at physiological temperature (37°C) were used as a reference for the normalization of cytoplasmic fluorescence. For ATP depletion studies, cells were incubated for 30 min at 37°C in glucose-free DMEM (Invitrogen) containing 10% FBS and supplemented with 10 mmol/L sodium azide and 6 mmol/L 2-deoxy-d-glucose (Sigma-Aldrich), a protocol described in more detail in a previous report.[39] After this treatment, the energy depletion medium was replaced by normal medium.

EM

Cell samples were fixed in 1.5% glutaraldehyde in 0.1 M cacodylate buffer (pH 7.4) for 1.5 h at room temperature. The samples were post-fixed in 1% osmium tetroxide in 0.1 M sodium-cacodylate solution for 2 h and stained overnight at 4°C in an aqueous uranyl acetate solution (1% in volume). After several washes in MQ water, the samples were dehydrated in a graded ethanol series and embedded in EPON resin. Sections of approximately 70 nm were cut with a diamond knife on a Leica EM UC6 ultramicrotome and images were collected with a JEOL JEM 1011 electron microscope operated at 100 keV equipped with a Gatan Orius SC1000 series CCD camera. For negative staining experiments, samples suspended in watery solutions were diluted to approximately 0.1 mg/mL with MQ water. Then 7 μL of sample suspensions were deposited (adsorption time = 60 s) on carbon film-coated 300 mesh copper grids (Electron Microscopy Sciences) after 60 s of treatment with plasma cleaner. Before TEM observation, negative staining was done on drops of 10 μL of 1% uranyl acetate in water for 60 s before grids drying. For cryo-EM, vitrification of samples was performed in liquid ethane cooled at liquid nitrogen temperature using the FEI Vitrobot Mark IV semiautomatic cryo-plunger (FEI Company). Bright-field cryo-EM was run at −176°C in an FEI Tecnai G2 F20 transmission electron microscope (FEI Company), working at an acceleration voltage of 200 kV and equipped, relevant for this project, with a field emission gun and automatic cryo-box. The images have been acquired in a low dose modality with a GATAN Ultrascan 1000 2k × 2k CCD.

FLIM

FLIM on CHO-K1 cells was performed by using a Leica TCS SP5 confocal microscope (Leica Microsystems). The samples were illuminated by a pulsed diode laser operating at 40 MHz with an excitation wavelength of 470 nm. The emission was collected in the 510- to 660-nm range by a photomultiplier tube interfaced with a time-correlated single photon counting card (PicoHarp 300, PicoQuant). The phasor analysis of experimental lifetime acquisitions was performed by using a dedicated routine of SimFCS software (Laboratory for Fluorescence Dynamics, University of California, Irvine). Technically, for each pixel in the image, the fluorescence decays measured in the time domain are mapped onto the so-called phasor plot, where a phasor has two coordinates: the real and imaginary parts of the Fourier transform of the fluorescence lifetime decay (with the area under the curve normalized at 1), calculated at the angular repetition frequency of the measurement. The phasors stay within the so-called universal (semi)circle centered at ($^1/_2$,0) with radius 0.5 and positive x, where the zero lifetime is located at (1,0) and the infinite lifetime at (0,0). This suggests that, by taking the Fourier transform of a measured decay curve, the lifetime can be estimated based on the position of the phasor inside the universal (semi)circle. The distribution of phasor points originating from FLIM measurements appears on the universal (semi)circle for mono-exponential decays or inside the (semi)circle for multi-exponential decays. FLIM on MCF10A and MDA-MB-231 cells was performed with the Olympus FluoView FV1000 system described above. Lifetime acquisition was made possible by means of a Fast-FILM box (ISS, Inc). The lifetime calibration was performed with a solution of Coumarin 6 diluted in ethanol (2.5 ns).

Phasor analysis of lifetime data

FLIM intensity measurements were analyzed with the SimFCS software (Laboratory for Fluorescence Dynamics, University of California, Irvine). To distinguish cytoplasm and nucleus, intensity images were used to draw the region of interest or to cut low signal outside cells. Several reference points were indicated in phasor plots using the following color code: black for cell autofluorescence (extracted from untreated cells), gray for L-DOX (batch used in our experiments), blue for DOX crystal (nanorod-shaped crystal inside liposomes, also visible in TEM) at 0.2 ns on the universal circle,[14] green for free DOX in aqueous solution at 1.0 ns on the universal circle according to literature, and red for DOX associated to the lipid membrane at 4.5 ns on the universal circle.[14]

Production of DOX aggregates

The production of DOX-crystal derivatives with a bottom-up approach required the use of a dimerization protocol.[25] In detail, a stock of F-DOX hydrochloride (2 mg/mL in water) was dissolved in an equal volume of DPBS (no calcium, no magnesium, pH 7.0–7.3) and incubated at 37°C for more than 24 h to gradually form a red precipitate. This doxorubicin precipitate was separated by centrifugation and resuspended in water, repeating this solubilization cycle four times. Doxorubicin aggregates can be obtained also by a top-down approach from pristine L-DOX. To induce liposome fragmentation, ultrasonic homogenization (sonication) was performed with the ultrasonic homogenizer BANDELIN SONOPULS HD2070 (20 kHz). In particular, a solution of L-DOX, diluted to a final concentration of 120 μg/mL total doxorubicin, was sonicated at the maximum power for 10 min in ice (with a few pauses to mitigate the temperature rise). Phasor FLIM fingerprints of the obtained solutions were acquired both in solution (after production) and in cells.

DATA AND CODE AVAILABILITY

Data available on request from the authors.

SUPPLEMENTAL INFORMATION

Supplemental information can be found online at https://doi.org/10.1016/j.omton.2024.200836.

ACKNOWLEDGMENTS

The authors acknowledge the support from the following funds: FLASH project for the valorization of patents through the Proof of Concept "JUMP 2023" program (financed by MIMiT within the PNRR), and project ECS00000017 'Ecosistema dell'Innovazione' Tuscany Health Ecosystem (THE, PNRR, Spoke 4: Nanotechnologies for diagnosis and therapy) from the European Union-Next Generation EU, MIUR PRIN Grant (2017YF9FBS). This work was supported by the Open Access Publishing Fund of the Scuola Normale Superiore.

AUTHOR CONTRIBUTIONS

A.C. performed all confocal and FLIM experiments, analyzed data, wrote a manuscript draft; A.M. and G.S. contributed to *in cuvette* experiments, analyzed data; D.D., F.Catalano, and R.M. performed electron microscopy experiments, analyzed data; V.P. realized the graphical model, discussed data; G.T. performed viability tests, discussed data; L.S. analyzed data, discussed data; D.P. provided materials, wrote a manuscript draft; G.C. designed research, discussed data, wrote the manuscript; F.B. discussed data, wrote the manuscript; F.Cardarelli designed and supervised research, analyzed data, and wrote the manuscript.

DECLARATION OF INTERESTS

The authors declare no competing interests.

REFERENCES

1. Gregoriadis, G. (1981). Targeting of drugs: implications in medicine. Lancet *2*, 241–246. https://doi.org/10.1016/S0140-6736(81)90486-4.

2. Barenholz, Y. (2012). Doxil® - The first FDA-approved nano-drug: Lessons learned. J. Control. Release *160*, 117–134. https://doi.org/10.1016/j.jconrel.2012.03.020.

3. Symon, Z., Peyser, A., Tzemach, D., Lyass, O., Sucher, E., Shezen, E., and Gabizon, A. (1999). Selective delivery of doxorubicin to patients with breast carcinoma metastases by stealth liposomes. Cancer *86*, 72–78. https://doi.org/10.1002/(SICI)1097-0142(19990701)86:1<72::AID-CNCR12>3.0.CO;2-1.

4. Maeda, H., Wu, J., Sawa, T., Matsumura, Y., and Hori, K. (2000). Tumor vascular permeability and the EPR effect in macromolecular therapeutics: a review. J. Control. Release *65*, 271–284. https://doi.org/10.1016/s0168-3659(99)00248-5.

5. Safra, T., Muggia, F., Jeffers, S., Tsao-Wei, D.D., Groshen, S., Lyass, O., Henderson, R., Berry, G., and Gabizon, A. (2000). Pegylated liposomal doxorubicin (doxil) Reduced clinical cardiotoxicity in patients reaching or exceeding cumulative doses of 500 mg/m2. Ann. Oncol. *11*, 1029–1033. https://doi.org/10.1023/a:1008365716693.

6. O'Brien, M.E.R., Wigler, N., Inbar, M., Rosso, R., Grischke, E., Santoro, A., Catane, R., Kieback, D.G., Tomczak, P., Ackland, S.P., et al. (2004). Reduced cardiotoxicity and comparable efficacy in a phase III trial of pegylated liposomal doxorubicin HCl (CAELYX™/Doxil®) versus conventional doxorubicin for first-line treatment of metastatic breast cancer. Ann. Oncol. *15*, 440–449. https://doi.org/10.1093/annonc/mdh097.

7. Judson, I., Radford, J.A., Harris, M., Blay, J.-Y., Van Hoesel, Q., Le Cesne, A., Van Oosterom, A.T., Clemons, M.J., Kamby, C., Hermans, C., et al. (2001). Randomised phase II trial of pegylated liposomal doxorubicin (DOXIL/CAELYX) versus doxorubicin in the treatment of advanced or metastatic soft tissue sarcoma: a study by the EORTC Soft Tissue and Bone Sarcoma Group. Eur. J. Cancer *37*, 870–877. https://doi.org/10.1016/S0959-8049(01)00050-8.

8. Rivera, E., Valero, V., Esteva, F.J., Syrewicz, L., Cristofanilli, M., Rahman, Z., Booser, D.J., and Hortobagyi, G.N. (2002). Lack of activity of stealth liposomal doxorubicin in the treatment of patients with anthracycline-resistant breast cancer. Cancer Chemother. Pharmacol. *49*, 299–302. https://doi.org/10.1007/s00280-001-0405-3.

9. Arta, A., Larsen, J.B., Eriksen, A.Z., Kempen, P.J., Larsen, M., Andresen, T.L., and Urquhart, A.J. (2020). Cell targeting strategy affects the intracellular trafficking of liposomes altering loaded doxorubicin release kinetics and efficacy in endothelial cells. Int. J. Pharm. *588*, 119715. https://doi.org/10.1016/j.ijpharm.2020.119715.

10. Seynhaeve, A.L.B., Dicheva, B.M., Hoving, S., Koning, G.A., and Ten Hagen, T.L.M. (2013). Intact Doxil is taken up intracellularly and released doxorubicin sequesters in the lysosome: Evaluated by in vitro/in vivo live cell imaging. J. Control. Release *172*, 330–340. https://doi.org/10.1016/j.jconrel.2013.08.034.

11. El-Hamid, E.S.A., Gamal-Eldeen, A.M., and Sharaf Eldeen, A.M. (2019). Liposome-coated nano doxorubicin induces apoptosis on oral squamous cell carcinoma CAL-27 cells. Arch. Oral Biol. *103*, 47–54. https://doi.org/10.1016/j.archoralbio.2019.05.011.

12. Shah, S., Chandra, A., Kaur, A., Sabnis, N., Lacko, A., Gryczynski, Z., Fudala, R., and Gryczynski, I. (2017). Fluorescence properties of doxorubicin in PBS buffer and PVA films. J. Photochem. Photobiol. B *170*, 65–69. https://doi.org/10.1016/j.jphotobiol.2017.03.024.

13. Zhu, S., Ma, L., Wang, S., Chen, C., Zhang, W., Yang, L., Hang, W., Nolan, J.P., Wu, L., and Yan, X. (2014). Light-scattering detection below the level of single fluorescent molecules for high-resolution characterization of functional nanoparticles. ACS Nano *8*, 10998–11006. https://doi.org/10.1021/nn505162u.

14. Tentori, P., Signore, G., Camposeo, A., Carretta, A., Ferri, G., Pingue, P., Luin, S., Pozzi, D., Gratton, E., Beltram, F., et al. (2022). Fluorescence lifetime microscopy unveils the supramolecular organization of liposomal Doxorubicin. Nanoscale *14*, 8901–8905. https://doi.org/10.1039/d2nr00311b.

15. Aminipour, Z., Khorshid, M., Keshvari, H., Bonakdar, S., Wagner, P., and Van der Bruggen, B. (2020). Passive permeability assay of doxorubicin through model cell membranes under cancerous and normal membrane potential conditions. Eur. J. Pharm. Biopharm. *146*, 133–142. https://doi.org/10.1016/j.ejpb.2019.10.011.

16. Düzgüneş, N., and Nir, S. (1999). Mechanisms and kinetics of liposome-cell interactions. Adv. Drug Delivery Rev. *40*, 3–18. https://doi.org/10.1016/s0169-409x(99)00037-x.

17. Cardarelli, F., Beltram, F., Tentori, P.M., Caracciolo, G., and Pozzi, D. (2022). Determination of the Supramolecular Organization of Encapsulated Molecules by Luminescence Lifetime (Google Patents).

18. Vallmitjana, A., Dvornikov, A., Torrado, B., Jameson, D.M., Ranjit, S., and Gratton, E. (2020). Resolution of 4 components in the same pixel in FLIM images using the phasor approach. Methods Appl. Fluoresc. *8*, 035001. https://doi.org/10.1088/2050-6120/ab8570.

19. Vallmitjana, A., Lepanto, P., Irigoin, F., and Malacrida, L. (2022). Phasor-based multi-harmonic unmixing for in-vivo hyperspectral imaging. Methods Appl. Fluoresc. *11*, 014001. https://doi.org/10.1088/2050-6120/ac9ae9.

20. Basuki, J.S., Duong, H.T.T., Macmillan, A., Erlich, R.B., Esser, L., Akerfeldt, M.C., Whan, R.M., Kavallaris, M., Boyer, C., and Davis, T.P. (2013). Using fluorescence lifetime imaging microscopy to monitor theranostic nanoparticle uptake and intracellular doxorubicin release. ACS Nano *7*, 10175–10189. https://doi.org/10.1021/nn404407g.

21. Chen, N.T., Wu, C.Y., Chung, C.Y., Hwu, Y., Cheng, S.H., Mou, C.Y., and Lo, L.W. (2012). Probing the Dynamics of Doxorubicin-DNA Intercalation during the Initial Activation of Apoptosis by Fluorescence Lifetime Imaging Microscopy (FLIM). PLoS One *7*, e44947. https://doi.org/10.1371/journal.pone.0044947.

22. Chen, E., Chen, B.M., Su, Y.C., Chang, Y.C., Cheng, T.L., Barenholz, Y., and Roffler, S.R. (2020). Premature Drug Release from Polyethylene Glycol (PEG)-Coated Liposomal Doxorubicin via Formation of the Membrane Attack Complex. ACS Nano *14*, 7808–7822. https://doi.org/10.1021/acsnano.9b07218.

23. Carretta, A., and Cardarelli, F. (2023). Monitoring drug stability by label-free fluorescence lifetime imaging: a case study on liposomal doxorubicin. J. Phys. Conf. Ser. *2579*, 012009. https://doi.org/10.1088/1742-6596/2579/1/012009.

24. Yamamoto, E., Hosogi, N., Takechi-Haraya, Y., Izutsu, K.I., Uchiyama, N., and Goda, Y. (2023). Folded, undulating, and fibrous doxorubicin sulfate crystals in liposomes. Nanomedicine *47*, 102631. https://doi.org/10.1016/j.nano.2022.102631.

25. Yamada, Y. (2020). Dimerization of Doxorubicin Causes Its Precipitation. ACS Omega *5*, 33235–33241. https://doi.org/10.1021/acsomega.0c04925.

26. Zhu, L., Yang, S., Qu, X., Zhu, F., Liang, Y., Liang, F., Wang, Q., Li, J., Li, Z., and Yang, Z. (2014). Fibril-shaped aggregates of doxorubicin with poly-l-lysine and its derivative. Polym. Chem. *5*, 5700–5706. https://doi.org/10.1039/c4py00686k.

27. Speelmans, G., Staffhorst, R.W., De Kruijff, B., and De Wolf, F.A. (1994). Transport Studies of Doxorubicin in Model Membranes Indicate a Difference in Passive Diffusion across and Binding at the Outer and Inner Leaflets of the Plasma Membrane. Biochemistry *33*, 13761–13768. https://doi.org/10.1021/bi00250a029.

28. Tacar, O., Sriamornsak, P., and Dass, C.R. (2013). Doxorubicin: An update on anticancer molecular action, toxicity and novel drug delivery systems. J. Pharm. Pharmacol. *65*, 157–170. https://doi.org/10.1111/j.2042-7158.2012.01567.x.

29. Borišev, I., Mrdanovic, J., Petrovic, D., Seke, M., Jović, D., Srdenović, B., Latinovic, N., and Djordjevic, A. (2018). Nanoformulations of doxorubicin: How far have we come and where do we go from here? Nanotechnology *29*, 332002. https://doi.org/10.1088/1361-6528/aac7dd.

30. Yang, F., Teves, S.S., Kemp, C.J., and Henikoff, S. (2014). Doxorubicin, DNA torsion, and chromatin dynamics. Biochim. Biophys. Acta Rev. Canc *1845*, 84–89. https://doi.org/10.1016/j.bbcan.2013.12.002.

31. Shen, F., Chu, S., Bence, A.K., Bailey, B., Xue, X., Erickson, P.A., Montrose, M.H., Beck, W.T., and Erickson, L.C. (2008). Quantitation of doxorubicin uptake, efflux, and modulation of multidrug resistance (MDR) in MDR human cancer cells. J. Pharmacol. Exp. Therapeut. *324*, 95–102. https://doi.org/10.1124/jpet.107.127704.

32. Lin, X.P., Mintern, J.D., and Gleeson, P.A. (2020). Macropinocytosis in different cell types: Similarities and differences. Membranes *10*, 177. https://doi.org/10.3390/membranes10080177.

33. Yang, J., Yin, Z., Chang, Y., Wang, H., Xu, J.F., and Zhang, X. (2021). Tumor acidity-induced charge-reversal liposomal doxorubicin with enhanced cancer cell uptake and anticancer activity. Giant *6*, 100052. https://doi.org/10.1016/j.giant.2021.100052.

34. Bernardi, M., Signore, G., Moscardini, A., Pugliese, L.A., Pesce, L., Beltram, F., and Cardarelli, F. (2023). Fluorescence Lifetime Nanoscopy of Liposomal Irinotecan Onivyde: From Manufacturing to Intracellular Processing. ACS Appl. Bio Mater. *6*, 4277–4289. https://doi.org/10.1021/acsabm.3c00478.

35. Caracciolo, G., Palchetti, S., Digiacomo, L., Chiozzi, R.Z.Z., Capriotti, A.L., Amenitsch, H., Tentori, P.M., Palmieri, V., Papi, M., Cardarelli, F., et al. (2018). Human Biomolecular Corona of Liposomal Doxorubicin: The Overlooked Factor in Anticancer Drug Delivery. ACS Appl. Mater. Interfaces *10*, 22951–22962. https://doi.org/10.1021/acsami.8b04962.

36. Fugit, K.D., Xiang, T.X., Choi, D.H., Kangarlou, S., Csuhai, E., Bummer, P.M., and Anderson, B.D. (2015). Mechanistic model and analysis of doxorubicin release from liposomal formulations. J. Control. Release *217*, 82–91. https://doi.org/10.1016/j.jconrel.2015.08.024.

37. Yamamoto, E., Hyodo, K., Suzuki, T., Ishihara, H., Kikuchi, H., and Kato, M. (2018). Simulation of Stimuli-Responsive and Stoichiometrically Controlled Release Rate of Doxorubicin from Liposomes in Tumor Interstitial Fluid. Pharm. Res. (N. Y.) *35*, 103. https://doi.org/10.1007/s11095-018-2380-y.

38. Nguyen, L.N.M., Lin, Z.P., Sindhwani, S., MacMillan, P., Mladjenovic, S.M., Stordy, B., Ngo, W., and Chan, W.C.W. (2023). The exit of nanoparticles from solid tumours. Nat. Mater. *22*, 1261–1272. https://doi.org/10.1038/s41563-023-01630-0.

39. Cardarelli, F., Serresi, M., Bizzarri, R., Giacca, M., and Beltram, F. (2007). In vivo study of HIV-1 tat arginine-rich motif unveils its transport properties. Mol. Ther. *15*, 1313–1322. https://doi.org/10.1038/sj.mt.6300172.